Comparative Analysis of Two Approaches for Multipath Ghost Suppression in Radar Imaging

G. Gennarelli, G. Vivone, P. Braca, F. Soldovieri, *Senior Member, IEEE*, and M. G. Amin, *Fellow, IEEE*

***Abstract*—Radar imaging is typically based on linear models of the electromagnetic scattering phenomenon. These models are robust and computationally efficient, but do not account for mutual interactions among targets in the scene as well as between the targets and surrounding environment. As a result, the radar images are characterized by spurious targets, i.e., multipath ghosts, which appear at positions where no physical targets exist. In this work, we compare two key approaches for clutter suppression. The first approach applies multiplicative fusion of the images corresponding to sub-apertures of the deployed array, whereas the second approach is based on coherence factor filtering, which enhances the image quality by suppressing low-coherence features. We assess the performance of these two methods in terms of imaging and detection capabilities. Numerical results based on synthetic data are reported to support the comparative analysis.**

***Index Terms*—Radar imaging, multipath ghosts, image fusion.**

I. Introduction

Target detection and localization based on knowledge of the scattered electromagnetic (EM) field remain the primary goals in radar imaging applications. Most radar imaging approaches are founded on linearized models of the EM scattering phenomena [1]. These models allow a qualitative description of the targets (i.e. location and approximate shape) by means of robust and computationally efficient data processing algorithms. Several data processing strategies have been proposed in the literature [1].

Linear models describe only direct scattering [2], thereby neglecting the scene multipath effects related to target-to-target and target-environment interactions. These multipath contributions produce spurious objects in the reconstructed images, thus increasing clutter and false alarms. Multipath signals and their ghosting effects can be exploited [3]-[11], possibly enhancing the signal-to-clutter ratio and the spatial resolution [5], [8]. These methods, which assume prior knowledge of the scene layout and model multipath propagation, have been proposed in the context of through-wall radar imaging and urban sensing.

Strategies to mitigate, or effectively remove, multipath ghosts are also of interest. They become crucial in the absence of any prior information about the scene or its major scatterers and under strong mutual target interactions. Ghost mitigation strategies can be based on ghost phase delays of the radar returns [12], the aspect dependent characteristics of multipath ghosts by sub-aperture imaging [13]-[15], or the analysis of range Doppler smearing due to multipath [16]. Recently, it has been shown that multipath ghosts can be effectively mitigated by a multiplication fusion of subarray images [17]. However, this approach suffers from the drawback of suppressing weak scattering targets, thereby impairing the image interpretations. Another popular approach is the coherence factor (CF) filtering that mitigates clutter by suppressing its low-coherence features [18], [19]. These two approaches have never been comparatively assessed.

Building on the results reported in [17], this letter presents a performance evaluation of the aforementioned approaches for clutter rejection. The multiplicative subarray image fusion (MSIF) approach is compared to the CF filtering approach by resorting to suitable image performance metrics. The classical ordered statistic constant false alarm rate (OS-CFAR) detector [20] is applied to compare the strategies in terms of target detection rate (DR) and false alarm rate (FAR).

II. Radar Imaging Model and Inversion Approach

Consider the 2D geometry depicted in Fig. 1. Without loss of generality, the background is assumed to be free-space. In general, more complex scenarios can be accounted for by resorting to pertinent electromagnetic modeling [1], [2]. Several targets, supposed metallic, are located in the investigation domain D, which is probed by an antenna array (either synthetic or a physical aperture) directed along x and covering the interval Γ of length L_x. The array operates in a multimonostatic mode, i.e., the scattered field is collected at the same location of the source. A wideband operation in the frequency range $\Omega = [\omega_{min}, \omega_{max}]$ is considered. Each source is modeled as a filamentary electric current directed along the y-axis (TM polarization), so that the problem at hand is scalar. The source/receiver positions are denoted by $\underline{r}_s$, and $\underline{r}$ is a generic point in D. Figure 1 illustrates multipath phenomena arising in the presence of several close targets.

Under Physical Optics (PO) approximation, a linear scattering model is established [17], [21]:

G. Gennarelli and F. Soldovieri are with the Institute for Electromagnetic Sensing of the Environment, National Research Council of Italy (CNR), 80124 Napoli, Italy.

G. Vivone and P. Braca are with the North Atlantic Treaty Organization (NATO) Science and Technology Organization (STO) Centre for Maritime Research and Experimentation, 19126 La Spezia, Italy.

M. G. Amin is with the Center for Advanced Communications, Villanova University, Villanova, PA 19085 USA.

Corresponding author: gennarelli.g@irea.cnr.it.

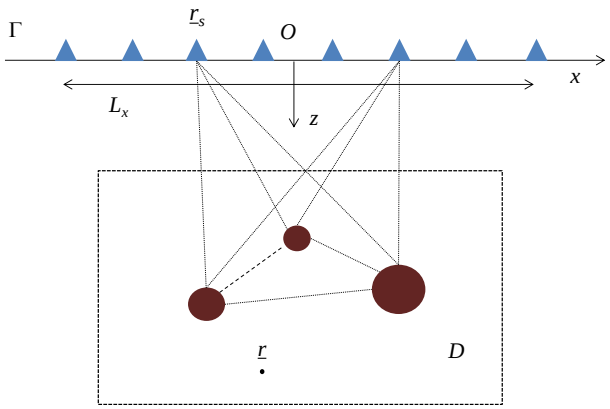

Fig. 1 Geometry of the problem. Multipath phenomena occur in the investigation region *D* due to the interactions among the targets.

$$E_s(\underline{r}_s,\omega) = \int_\tau G(\underline{r}_s,\underline{r},\omega)E_i(\underline{r}_s,\underline{r},\omega)\gamma(\underline{r})d\tau = L\gamma \qquad (1)$$

where E_s is the scattered field (datum), G is the free-space Green's function, E_i is the incident field in D, and γ is a distribution (unknown) supported over $\tau = \bigcup_i \tau_i$, i.e., the union of target contours τ_i. The operator notation has been introduced in (1), where the linear operator $L: X \to Y$ maps the space of unknown X into data space Y.

Different methods can be applied to invert the problem (e.g. see [1], [22]). In this work, we consider the common inversion scheme based on the adjoint operator L^*, i.e.,

$$\gamma = L^* E_s \qquad (2)$$

which is basically equivalent to beamforming or matched filtering. The spatial map defined by the magnitude of γ is referred as tomographic image and denoted as I.

As shown in [17], the scattered field is the superposition of direct scattering contributions and multipath terms. The former are responsible for the reconstruction of true targets in the scene, whereas the latter are associated with false targets. Multipath ghosts are typically defocused with respect to the true targets and are located at positions where no physical target exists. Most notably, according to [13]-[15], multipath ghosts exhibit aspect dependent characteristics. Thus, a different behavior in ghost reconstructions (i.e., location and shape) is observed when partitioning the radar aperture into smaller subarrays. This enables ghost suppression by fusion of subarray images [17].

III. Multipath Ghost Suppression Strategies and Performance Criteria

This Section discusses the two multipath ghost mitigation approaches and defines performance criteria for comparison.

A. MSIF approach

Following [17], the radar aperture is partitioned into N subarrays and a tomographic image I_n is obtained from each subarray dataset via (2). Then, a composite ghost-free image I^{MSIF} is obtained by a pixel-by-pixel multiplicative fusion of magnitude images related to each subarray [23], i.e.

$$I^{MSIF}(\underline{r}) = \prod_{n=1}^{N} I_n(\underline{r}) \quad \underline{r} \in D \qquad (3)$$

For convenience, I^{MSIF} is normalized with respect to its maximum value. As shown in [17], the MSIF approach defined by (3) offers the possibility to attenuate spurious targets; however, weak objects may be also suppressed.

B. CF filtering approach

CF filtering is an imaging tool that has been first applied in ultrasonic imaging [18] and recently employed in through wall radar imaging [19]. CF measures the coherence of signals scattered from a generic point in the investigation domain D and is defined as the ratio between the total coherent power received by the radar aperture to the total incoherent power. Define

$$y_m(\underline{r}) = \int_{\omega_{min}}^{\omega_{max}} E_s(\underline{r}_{sm},\omega)\, e^{j2k|\underline{r}-\underline{r}_{sm}|} d\omega \qquad (4)$$

as the downrange profile of the scattered field E_s where M is the total number of measurement points located at $\underline{r}_{sm}$, $m = 1,\dots M$. The CF is expressed as

$$CF(\underline{r}) = \frac{\left|\sum_{m=1}^{M} y_m(\underline{r})\right|^2}{M\sum_{m=1}^{M}\left|y_m(\underline{r})\right|^2} \quad \underline{r} \in D \qquad (5)$$

The spatial map defined by $CF(\underline{r})$ varies from zero to one and provides information about the low and high coherence regions in the investigated domain. The CF enhanced image I^{CF} is obtained by applying the CF function to the tomographic image I provided by adjoint inversion, i.e.

$$I^{CF}(\underline{r}) = CF(\underline{r})I(\underline{r}) \quad \underline{r} \in D \qquad (6)$$

According to (6), features with low coherence such as multipath ghosts are suppressed, or significantly attenuated, in the image. Note that, similar to the multiplicative fusion, CF could also be calculated using the same N subarrays where the coherent result from each subarray is then combined coherently and non-coherently to form a composite CF. However, this approach reduces the non-coherent terms in the denominator and is, therefore, inferior to the form in (5).

C. Imaging performance metrics

Two different metrics are used to compare the performance of the two strategies in terms of image quality [23]. The first metric is the improvement factor (IF) in the target-to-clutter ratio (TCR), defined as

$$IF = 10\, log_{10}\left(\frac{TCR_{out}}{TCR_{in}}\right) \qquad (7)$$

where $TCR_{in,out} = Pt_{in,out}/Pc_{in,out}$, and Pt and Pc denote the average target and clutter powers, respectively. The subscript "*in*" refers to the image when only adjoint inversion is carried out according to (2). The subscript "*out*" refers to the image achieved after the application of a ghost mitigation strategy (MSIF or CF). Note that the IF parameter describes the

enhancement in the overall image.

The second figure of merit, more suitable for weak scatterers, is the target improvement factor (TIF)

$$TIF = 10\, log_{10}\left(\frac{Pt_{out}}{Pt_{in}}\right) \tag{8}$$

which quantifies the improvement of the target power (Pt). Since the goal is to analyze performances in known scenarios, the IF and TIF parameters are evaluated over the regions of interest (RoI) containing the true targets. It is feasible to compute the target and clutter powers involved in (7) and (8). Specifically, the average power in a target or clutter region $R_{t,c}$ of the composite image I is defined as

$$P_{t,c} = \frac{1}{Q_{t,c}} \sum_{q=1}^{Q_{t,c}} I_q^2(\underline{r}) \qquad \underline{r} \in R_{t,c} \tag{9}$$

where $Q_{t,c}$ is the number of pixels belonging to $R_{t,c}$.

D. Detection performance

The classical OS-CFAR detector [20] is implemented to evaluate the detection performance of the MSIF and the CF strategies. Such a detector works as follows. The square amplitude of each pixel in a tomographic image is compared to a threshold, which depends on the estimated noise level and nominal P_{FA}. The observations in the reference window are sorted to form a sequence in ascending numerical order $\{ I_{(1)}, I_{(2)}, \dots, I_{(N_c)}\}$, where N_c is the number of cells in the reference window. The k-th order statistic $I_{(k)}$ is selected as representative of the interference level, and the threshold is set as $T_h = \alpha\, I_{(k)}$. For a square-law detector and additive white Gaussian noise (AWGN) on the real and imaginary parts of the complex image reconstruction, the clutter in the tomographic image I has an exponential distribution. As a result, the constant α is evaluated from the nominal P_{FA} as

$$P_{FA} = k\, \frac{N_c!}{k!\,(N_c-k)!} \frac{(k-1)!(\alpha+N_c-k)!}{(\alpha+N_c)!} \tag{10}$$

The receiver operating characteristic (ROC) curves are evaluated to examine the performance of the ghost mitigation approaches. To this end, the nominal P_{FA} is varied, and so is the threshold T_h, which implies a simultaneous variation of DR and FAR. As done in [23], the DR is computed as the percentage of pixels detected in the RoI, i.e., where true targets are present, while the FAR is calculated as the percentage of pixels detected in the clutter region.

IV. Numerical Results

The measurement array, depicted in Fig. 2, covers the interval [−1.5, 1.5] m, and the spacing between the measurement points is fixed at 0.0375 m (81 measurement points). The operating frequency range of the system is [0.5, 1.5] GHz, and a frequency step of 50 MHz is considered for data inversion. The investigation domain D=[−1.0,1.0]× [0.5,2.0] m^2 is discretized into square image pixels with side 0.05 m. The scene is populated by three metallic cylinders

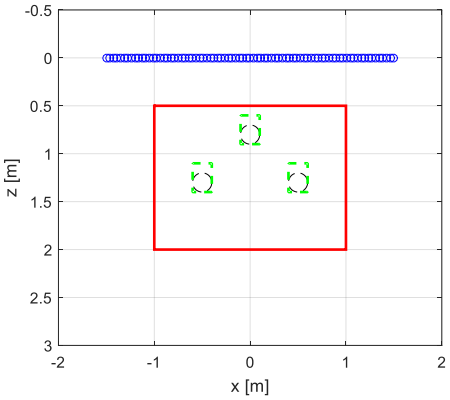

Fig. 2 Simulated scenario: measurement points (blue circles), investigation domain (red rectangle), targets (black circles), RoI (green rectangles).

having radius 0.1 m and centered at (−0.5, 1.25) m, (0, 0.75) m, and (0.5, 1.25) m, respectively.

The numerical tests exploit synthetic data generated by the GPRmax2D solver [24]. The scattered field in the frequency domain is computed from time-domain data after a time-gating operation to remove direct coupling between transmitting and receiving antennas. Finally, the frequency domain data are corrupted by AWGN.

The tomographic reconstruction depicted in Fig. 3 is obtained by standard adjoint-based inversion of data collected by the entire array. The signal-noise-ratio (SNR) on scattered field is assumed to be 0 dB. As can be seen, high intensity spots appear in correspondence of the upper edge of the targets since they are not penetrable. However, due to multiple scattering, the image is cluttered by lower intensity artifacts, which appear as spots located among the targets and at greater downrange (see red arrows in Fig. 3).

The reconstructions in Fig. 4 are obtained by applying the MSIF approach. To this end, the original array is partitioned into N contiguous and non-overlapping subarrays. In particular, we report the images achieved when N=2 (left panel), N=3 (center panel), and N=4 (right panel). It is evident that the images are much less cluttered than in Fig. 3 and multipath ghosts and noise are significantly attenuated. For N=2, the three targets are clearly distinguishable and only some residual clutter is present. However, as the number of subarrays increases (N>2), the clutter is totally suppressed, but the response of the two far targets is weakened so that their visual identification becomes difficult for the considered dynamic range. By increasing this range, all targets can be identified but with amplified clutter.

The image in Fig. 5 is obtained by adjoint inversion followed by the application of the CF approach. It can be observed that most of clutter in Fig. 3 is suppressed except for some residual artifacts. On the other hand, the real targets are clearly discernible, unlike for the MSIF approach with N=3, 4. Moreover, despite the symmetrical scene, lateral targets have different amplitude because data are affected by AWGN, which is not spatially symmetric.

In order to disengage from the specific realization of the AWGN, 200 Monte Carlo trials are performed for SNR values equal to −10, −5, 0, 5, 10 dB. For each value, the imaging performance metrics, introduced in Subsec. III C, are computed

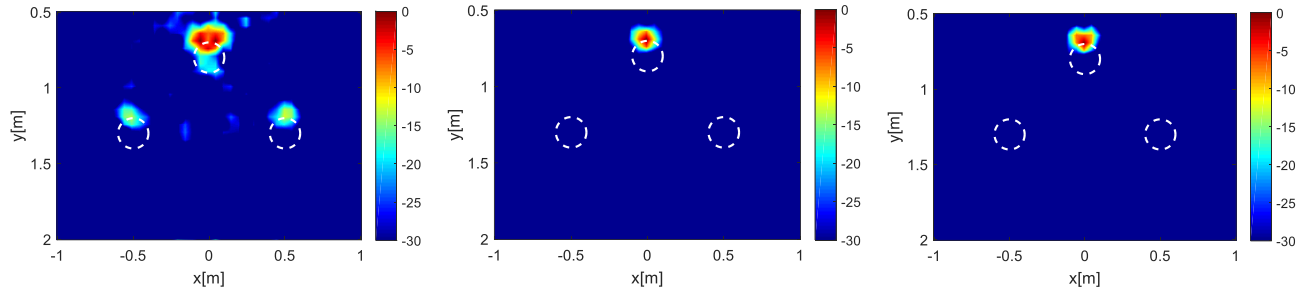

Fig. 4 Relative amplitude (dB) of the tomographic images achieved by adjoint inversion and MSIF when SNR on data is equal to 0 dB. $N = 2$ subarrays (left panel). $N = 3$ subarrays (center panel). $N = 4$ subarrays (right panel).

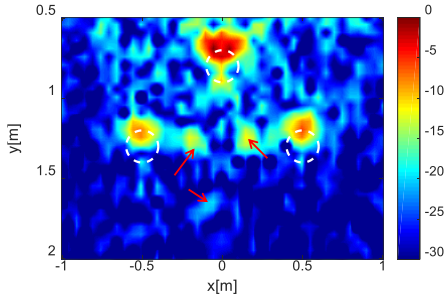

Fig. 3 Relative amplitude (dB) of the tomographic image achieved by adjoint inversion when SNR is 0 dB. Red arrows denote multipath ghosts.

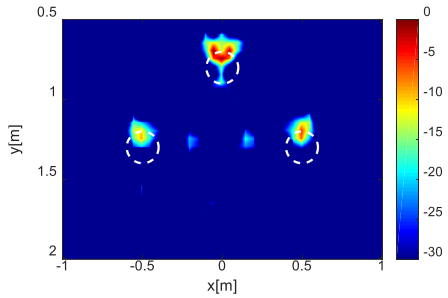

Fig. 5 Relative amplitude (dB) of the tomographic image achieved by adjoint inversion and CF filtering when SNR on data is equal to 0 dB.

and averaged over the trials.

The left panel of Fig. 6 displays the average *IF* versus SNR for both MSIF and CF filtering approaches. For the MSIF approach, the *IF* is computed for three different numbers of subarrays (N=2, 3, 4). For a fixed number of subarrays, *IF* decreases with SNR, with the more favorable situation (higher *IF*) occurring when N=4; this behavior is consistent with (7). Indeed, it is observed from the numerical results that the TCR_{out} is weakly dependent on the SNR whereas the TCR_{in}, based on adjoint inversion, significantly degrades as the SNR decreases.

The CF filtering exhibits a similar trend versus SNR. However, the achieved improvement in TCR is lower than that of the MSIF approach. This behavior is consistent with the tomographic image in Fig. 5, which highlights the presence of a slightly larger residual clutter with respect to the images in Fig. 4. Note that, for high SNRs, the CF filtering has a similar performance to the MSIF approach with N=2.

The curves, showing the average *TIF* versus SNR, are reported in the right panel of Fig. 6. A behavior almost independent of SNR is clearly observed for each strategy. This graph is informative since it underscores the fact that, for a fixed SNR, the target response achieved via MSIF approach degrades as the number of subarrays increases. The decreasing trend at low SNR values is justified by realizing that the power in the target regions after image fusion is almost independent of SNR; conversely, when only adjoint inversion is performed, the increase in power is an effect of the higher noise level. As a result, the ratio defined by (8) decreases. The CF filtering provides *TIF* values nearly intermediate between those achieved via MSIF approach for N=2 and N=3.

Finally, the detection performance is assessed from the ROC of the OS-CFAR detector. The 75th percentile is chosen to fix the threshold T_h [20]. The reference and guard windows sizes are 11×11 and 7×7 pixels, respectively. The DR and FAR are averaged over the Monte Carlo trials.

The ROC curves in left, center, and right panels of Fig. 7 refer to SNR values equal to −10, 0, +10 dB, respectively. It is seen that, when standard adjoint inversion is performed and no clutter rejection strategy is applied, the achievable detection rates are highly dependent on the noise level of the data, and increase with SNR for a fixed FAR. This result has a physical justification, since targets are less detectable when data are severely corrupted by noise and clutter. It is also seen that the MSIF approach significantly improves the DR with respect to standard adjoint inversion. This is particularly evident from the results achieved for SNR values equal to −10 and 0 dB. It is important to note that the DR values achieved with MSIF and CF filtering approach are comparable and almost independent of the SNR. This is due to the fact that the TCR and targets' power, after the application of MSIF and CF filtering, are not affected by the noise level in the data. However, for this example, MSIF approach using N=3 subarrays provides a slightly superior performance in terms of DR for all SNR values. This claim is supported by the areas under the ROC curve (AOC) values summarized in Tab. I.

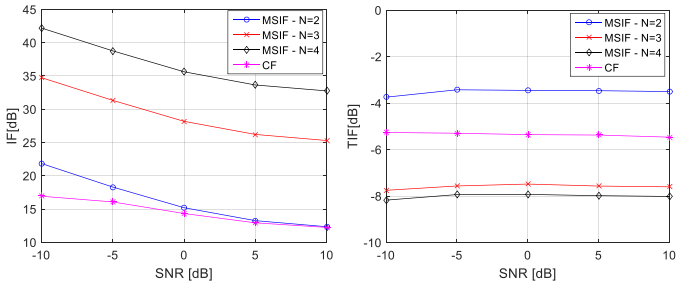

Fig. 6 Image performance metrics (dB) vs. SNR averaged over 200 Monte Carlo trials. *IF* (left panel). *TIF* (right panel).

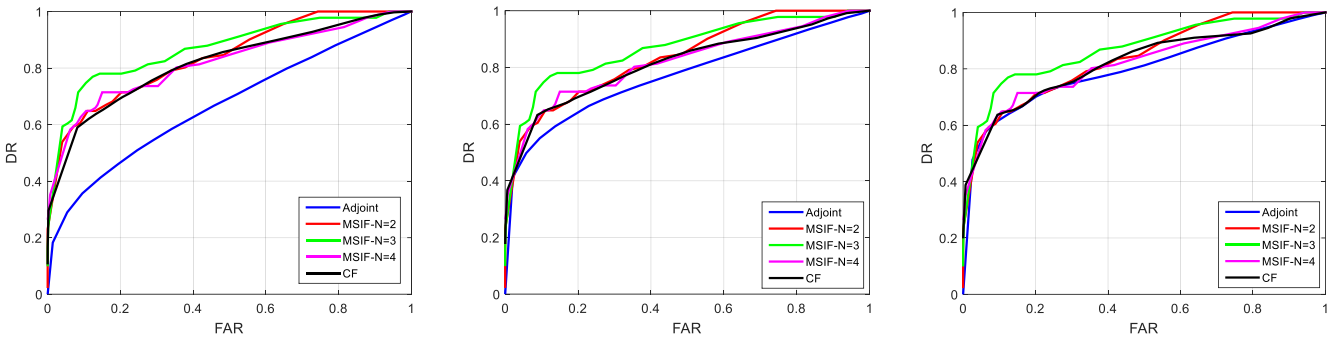

Fig. 7 ROC curves of the OS-CFAR detector for adjoint inversion, MSIF approach (N=2,3,4), and CF filtering strategies. SNR=−10 dB (left panel). SNR=0 dB (middle panel). SNR = +10 dB (right panel).

TABLE I
COMPARISON OF AOC VALUES FOR ADJOINT, MSIF, AND CF APPROACH

	SNR (dB)	Adjoint	MSIF (N=2)	MSIF (N=3)	MSIF (N=4)	CF
Three targets scenario	−10	0.67	0.84	0.87	0.82	0.82
	0	0.77	0.84	0.87	0.82	0.82
	+10	0.80	0.84	0.87	0.82	0.82
One target scenario	−10	0.76	0.90	0.90	0.84	0.88
	0	0.87	0.90	0.90	0.84	0.91
	+10	0.89	0.90	0.90	0.84	0.91

The above analysis has been repeated also for an asymmetric scenario with a single target located at (0.5, 1.25) m. Similar ROC curves (not shown) have been found with slightly higher DR values due to the absence of multipath clutter (Tab. I).

V. CONCLUSION

Two strategies for multipath clutter suppression, namely, the multiplicative subarray image fusion and the coherence factor filtering, were compared to conventional adjoint inversion. Their performance were assessed from both imaging and detection viewpoint. Multiplicative subarray image fusion notably improves the imaging quality, yielding lower clutter than coherence factor filtering; however, it tends to suppress weaker targets as the number of subarrays increases. It was found that multiplicative subarray image fusion and CF filtering are both robust to noise and have similar detection performance. Thus, they can be equivalently exploited to enhance target detectability in highly cluttered environments.

REFERENCES

[1] R. Solimene, I. Catapano, G. Gennarelli, A. Cuccaro, A. Dell'Aversano and F. Soldovieri, "SAR imaging algorithms and some unconventional applications: a unified mathematical overview," *IEEE Signal Process. Mag.*, vol. 31, no. 4, pp. 90-98, Jul. 2014.

[2] W. C. Chew, *Waves and Fields in Inhomogeneous Media*. New York, NY, 521 USA: IEEE Press, 1995.

[3] P. Setlur, M. Amin, and F. Ahmad, "Multipath model and exploitation in through-the-wall and urban radar sensing," *IEEE Trans. Geosci. Remote Sens.*, vol. 49, no. 10, pp. 4021-4034, Oct. 2011.

[4] P. C. Chang, R. J. Burkholder, and J. L. Volakis, "Model-corrected microwave imaging through periodic wall structures," *Int. J. Antennas Propag.*, vol. 2012, Article ID 948365, 7 pages, Mar. 2012.

[5] G. Gennarelli and F. Soldovieri, "A linear inverse scattering algorithm for radar imaging in multipath environments," *IEEE Geosci. Remote Sens. Lett.*, vol. 10, no. 5, pp. 1085-1089, Sept. 2013.

[6] G. Gennarelli, I. Catapano, and F. Soldovieri, "RF/microwave imaging of sparse targets in urban areas," *IEEE Antennas Wireless Propag. Lett.*, vol. 12, pp. 643–646, May 2013.

[7] P. Setlur, G. Alli, and L. Nuzzo, "Multipath exploitation in through-wall radar imaging via point spread functions," *IEEE Trans. Image Process*, vol. 22, no. 12, pp. 4571–4586, Dec. 2013.

[8] G. Gennarelli and F. Soldovieri, "Radar imaging through cinderblock walls: achievable performance by a model-corrected linear inverse scattering approach," *IEEE Trans. Geosci. Remote Sens.*, vol. 52, no. 10, pp. 6738–6749, Oct. 2014.

[9] G. Gennarelli, G. Riccio, R. Solimene, and F. Soldovieri, "Radar imaging through a building corner," *IEEE Trans. Geosci. Rem. Sens.*, vol. 52, no. 10, pp. 6750–6761, Oct. 2014.

[10] M. Leigsnering, M. Amin, F. Ahmad, and A. M. Zoubir, "Multipath exploitation and suppression for sar imaging of building interiors," *IEEE Signal Process. Mag.*, vol. 31, no. 4, pp. 110–119, Apr. 2014.

[11] G. E. Smith and B. G. Mobasseri, "Multipath exploitation for radar target classification," in *Proc. IEEE Radar Conf.*, Atlanta, GA, 2012, pp. 0623-0628.

[12] J. De Laurentis, "Multipath synthetic aperture radar imaging," *IET Radar Sonar Nav.*, vol. 5, no. 5, pp. 561–572, May 2011.

[13] W. Liang, H. Xiaotao, Z. Zhimin, and S. Qian, "Research on UWB SAR image formation with suppressing multipath ghosts," in *Proc. CIE Int. Conf. Radar*, Shanghai, 2006, pp. 1–3.

[14] A. T. Abdalla, A. H. Muqaibel, and S. Al-Dharrab, "Aspect dependent multipath ghost suppression in TWRI under compressive sensing framework," in *Proc. Int. Conf. on Communication Signal Processing and their Applications*, Sharjah, 2015, pp. 1-6.

[15] Q. Tan, H. Leung, Y. Song, and T. Wang, "Multipath ghost suppression for through-the-wall-radar," *IEEE Trans. Aerosp. Electron. Syst.*, vol. 50, no. 3, pp. 2284-2291, Jul. 2014.

[16] B. D. Rigling, "Urban RF multipath mitigation," *IET Radar Sonar Nav.*, vol. 2, no. 6, pp. 419-425, Jun. 2008.

[17] G. Gennarelli and F. Soldovieri, "Multipath ghosts in radar imaging: physical insight and mitigation strategies," *IEEE J. Sel. Topics Appl. Earth Observ. Remote Sens.*, vol. 8, no. 3, pp. 1078–1086, Mar. 2015.

[18] K. W. Hollman, K. W. Rigby, and M. O'Donnell, "Coherence factor of speckle from a multi-row probe," in *Proc. IEEE Ultrasonics Symp.*, Caesars Tahoe, NV, 1999, pp. 1257–1260.

[19] R. J. Burkholder and K. E. Browne, "Coherence factor enhancement of through-wall radar images," *IEEE Antennas Wireless Propag. Lett.*, vol. 9, pp. 842-845, Aug. 2010.

[20] H. Rohling, "Radar CFAR thresholding in clutter and multiple target situations," *IEEE Trans. Aerosp. Electron. Syst.*, vol. 19, no. 4, pp. 608–621, Jul. 1983.

[21] R. Pierri, A. Liseno, R. Solimene, and F. Soldovieri, "Beyond physical optics svd shape reconstruction of metallic cylinders," *IEEE Trans. Antennas Propag.*, vol. 54, no. 2, pp. 655–665, Feb. 2006.

[22] M. Bertero and P. Boccacci, *Introduction to inverse problems in imaging*. London, UK: IOP publishing, 1998.

[23] C. H. Seng, A. Bouzerdoum, M. G. Amin, and S. L. Phung, "Probabilistic fuzzy image fusion approach for radar through wall sensing," *IEEE Trans. Image Process.*, vol. 22, no. 12, pp. 4938–4951, Dec. 2013.

[24] A. Giannopoulos, *Gprmax 2d/3d v2.0 User's Manual*, Univ. Edinburgh, 2005.